Topic	**Animations as educational complements to NMSOP-2**
Authors	**Peter Bormann** (formerly GFZ German Research Centre for Geosciences, D-14473 Potsdam, Germany); E-mail: pb65@gmx.net
	Siegfried Wendt, Geophysical Observatory Collm, University of Leipzig, D-04779 Wermsdorf, Germany, E-mail: wendt@rz.uni-leipzig.de
	Ute Starke, Computer Center, University of Leipzig, Augustusplatz 10-11, 04109 Leipzig; E-mail: starke@rz.uni-leipzig.de
Version	November 2012; **DOI: 10.2312/GFZ.NMSOP-2_IS_1.1**

1 Introduction

NMSOP-2 has been amended by many new materials, including demonstrations and animations to topical chapters, exercises, information sheets etc. Animations visualize in an appealing and easy comprehensible way key aspects outlined in the main texts. They are made freely available for viewing and downloading. These complementary materials are suitable for being used independently of NMSOP as a whole as educational material at different levels, e.g., for "seismology at schools", which enjoys currently growing interest and support in many countries, in undergraduate university or on-the job training courses. Animation have proven to be useful and well received also by the audience in public lectures about Earth science including topics such as the nature and location of earthquakes by means of seismic recordings, the propagation of seismic waves through the Earth and their use for investigating the Earth structure. This is illustrated below by way of a several examples. IS 1.1 itself can be used as an introductory tutorial to the animations. With a view to a broad user spectrum we aim at a largely non-technical language and the introduction of all basic technical terms so that both this text and the animations can be understood also by interested pupil and layman.

The tutorials, demos and animations currently offered in NMSOP-2 are just a beginning. We sincerely hope that they will be further upgraded and significantly amended in future by additional ones on other topics, satisfying both specialized as well broader interests. Therefore, the Editor (first author) invites potential contributors to contact him and to make their related products available to the broad NMSOP user community. He will in turn arrange that these new contributions will be highlighted in and properly linked with the topically related NMSOP main texts, thus assuring their widest possible propagation and use.

2 Examples

2.1 Propagation of seismic rays through the Earth and the formation of seismic records

NMSOP-2 offers 10 animations which show the propagation of seismic rays of different seismic phases through the Earth as well as the formation of seismic records of these waves from earthquakes at different depth (from 10 to 600 km) at seismic stations of the German Regional Seismic Network (GRSN) or local networks at distances ranging from 0.1° to 167° (i.e., from about 10 km to over 18,000 km). These phases relate to both direct longitudinal (P) and transverse (S) body waves (see Figure 13) as well their (often multiply) reflected and/or converted versions. Rays are refracted, reflected and/or converted when interacting with velocity and density discontinuities or gradients in the Earth crust (e.g., the Conrad and Mohorovičić-discontinuity), or in the deeper Earth, such as the core-mantle boundary (see Figures 1 and 2).

Figure 3 shows a screen-shot of one of the seismic ray tracing and record animations for an earthquake in New Zealand, recorded at station MOX and other stations of the German Regional Seismic Network (GRSN) at epicentre distances between 160° and 167°. On the lower right a simplified Earth model with the mantle in turquoise, the outer core in lilac and the inner core in red. The generally gradual increase of seismic wave velocity with depth in the mantle causes the bending of the seismic rays and the strong decrease of wave velocity at the core-mantle boundary (CMB) from about 13 km/s in the lowermost mantle to 8 km/s in the uppermost core a pronounced refraction of the P waves into the core (see the turquoise ray). However, for rays that incident on the CMB at near vertical angles the refraction is negligible (see the dark blue ray through the inner core. Thus, the figure illustrates the dependence of the refraction angle on both the gradual (in the mantle) or discontinuous (CMB) change in velocity as well as on the incidence angle of seismic rays with respect to the velocity change with depth. And Figure 4 shows the currently best 1-D model AK 135 of velocity, density and attenuation related changes in the Earth according to Kennett et al. (1995) and Montagner and Kennett (1996). Such models have been derived by analyzing empirically determined travel-time curves of P, S and other seismic body waves as well as dispersion curves of surface waves.
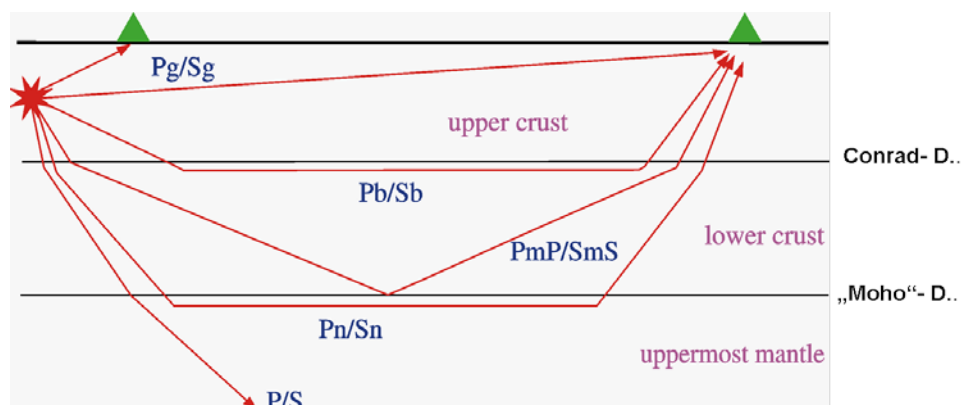

Figure 1 Simplified model of the crust showing ray traces of the main "crustal phases" observed in records of earthquakes at distances up to about 1000 km. The short term "Moho" stands for Mohorovičić-discontinuity. It is the boundary between the Earth crust and the Earth mantle, characterized by a strong increase in P-wave velocity from about 6.5 km/s to 8 km/s).
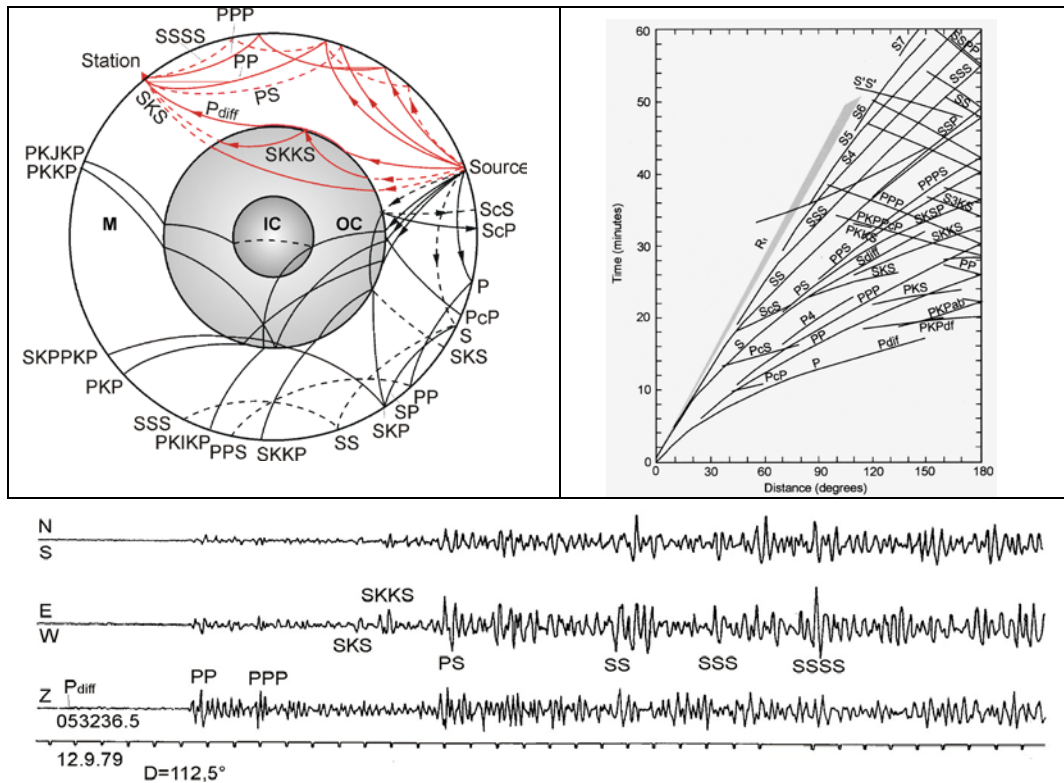
Figure 2 Top left: Seismic rays through the Earth mantle (**M**), outer core (**OC**) and inner core (**IC**) with their respective phase symbols according to international nomenclature. Full lines: P-wave rays; broken lines: S-wave rays. **Top-right:** Related travel-time curves of these phases. **Red rays** relate to the seismic phases identified in a 3-component broadband seismogram recorded at station MOX, Germany (**bottom**), from an earthquake at a distance of 112.5° (compiled from various Figures in Chapter 2).
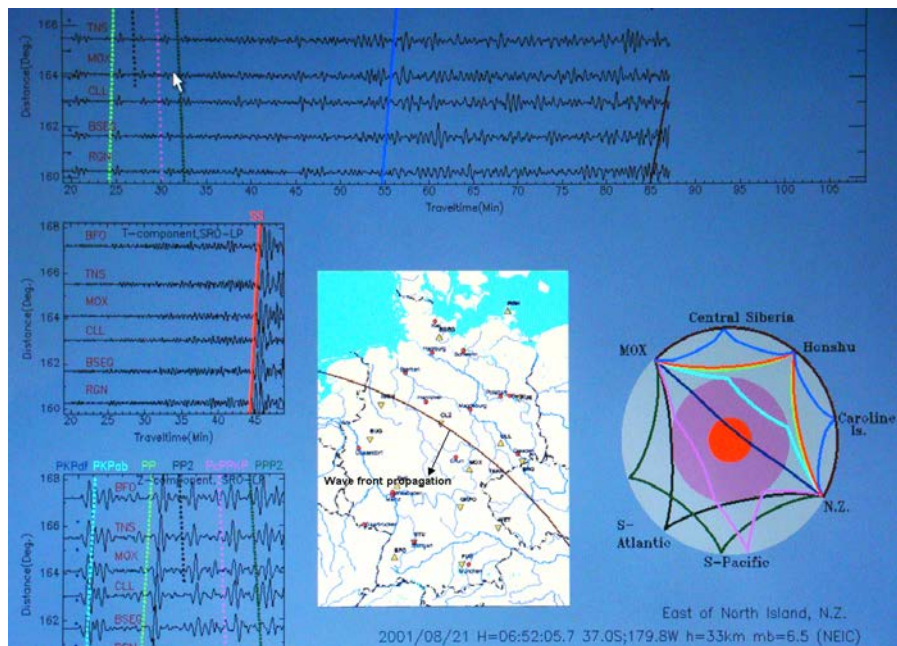
Figure 3 Screenshot of a moment towards the end of the first animation example, based on seismic recordings of the Mw = 7.1 New Zealand earthquake of 21 August 2001 at stations of the German Regional Seismic Network (GRSN). For more explanation see text.
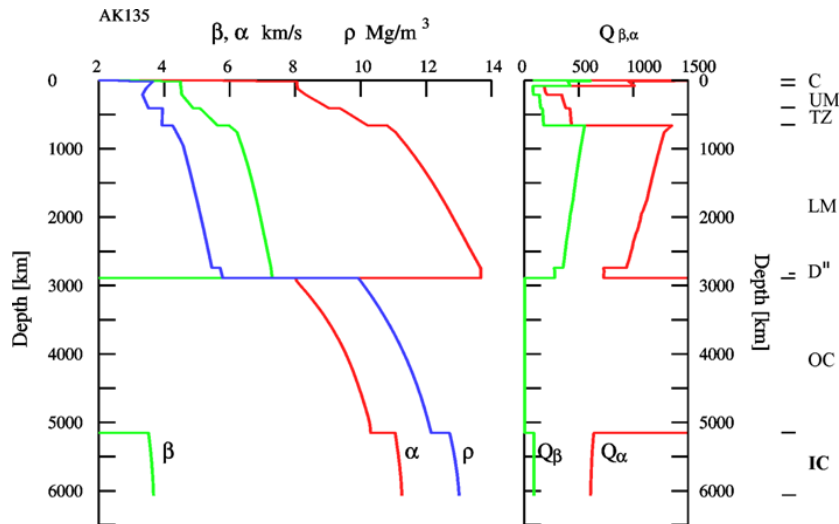
Figure 4 The 1-D Earth model AK135. Seismic wave speeds according to Kennett et al., 1995), quality parameter Q and density according to Montagner and Kennett (1996). $\alpha = v_P$ and $\beta = v_S$ are the P- and S-wave velocity, respectively; ρ - density, Q_α and $Q_\beta = Q_\mu$ the "quality factor" Q for P and S waves. Note that wave attenuation is proportional to 1/Q. The abbreviations on the outermost right stand, within the marked depth ranges, for: C – crust, UM – upper mantle, TZ – transition zone, LM – lower mantle, D"- gradient layer, OC – outer core, IC – inner core. (Copy of part of Fig. 2.79 in Chapter 2).

The ray-propagation cartoon in Figure 3, and with better resolution Figure 5, shows that seismic rays, the deeper they penetrated into the Earth, the steeper they return back to the Earth surface. And the steeper they come to the surface the shorter are the time differences at which the respective seismic waves will arrive at different seismic stations on the surface. But the shorter the difference between the recorded phase arrivals the faster this wave - **apparently** - seems to travel along the surface. This apparent horizontal velocity v_{app} of the approaching wave front (see the bended curve in the middle insert of Figure 3 with the arrow in the direction of propagation) should not be mistaken as being the true wave velocity. v_{app} will become infinite for vertical incidence although the real velocity of P and S near to the Earth surface is not larger than about 5 km/s and 3 km/s, respectively. The inverse of v_{app} is called *slowness* $= 1/v_{app}$. The animation will show that surface-waves, travelling along the Earth surface (bended brown ray) with less than 3-4 km/s, are indeed the slowest waves of all. Also note that seismic rays do not travel only the shortest way from the source towards the recording stations but also the longer one. Accordingly, for the same type of wave, the respective long-path wavefront arrives later and from the opposite direction with *negative slowness*, i.e., they arrive first at the most distant stations and later at the nearer ones. This results in travel-time branches of different tilt (see the colored lines on the record plots of Figure 5 which connect the arrival times of the respective seismic phases.)

In the animation three kinds of seismic records are "written" as soon as the seismic waves of different phases, represented by their differently colored seismic rays, arrive at the stations. All three have been long-period filtered with the SRO-LP response which emphasizes periods around 20 s. The uppermost record section in Figure 3 (and more clearly in Figure 5) shows vertical-component records, the middle section transverse-component records and the lowermost

record section shows enlarged in amplitude and with better time resolution the first 15 min of the uppermost record. The T-component records only shear-wave motions in the horizontal plane.
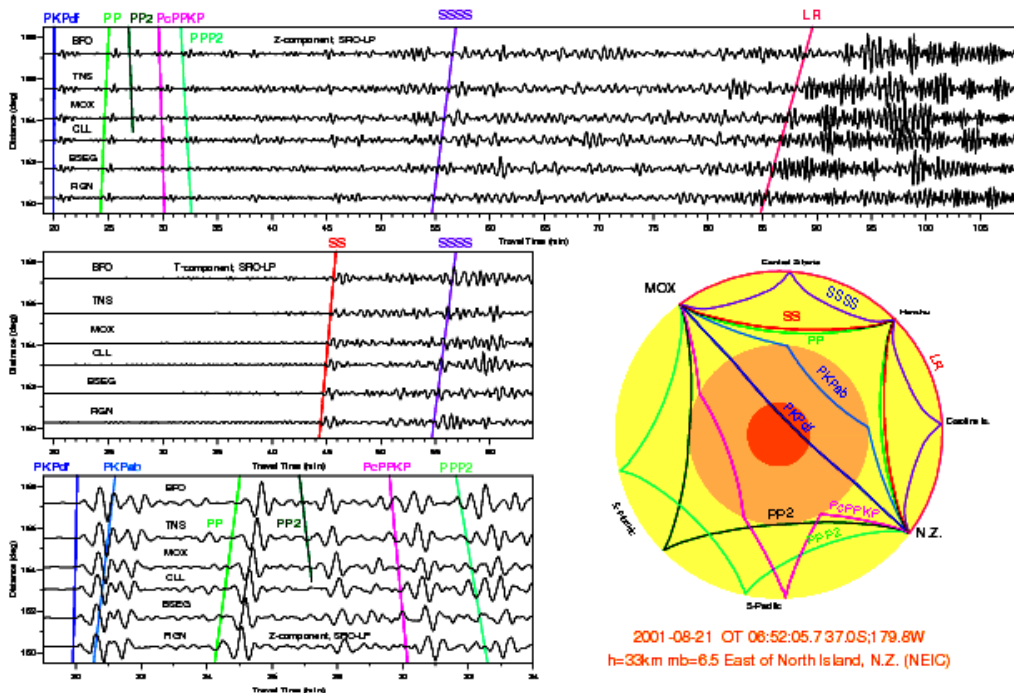
Figure 5 A modified version of Figure 3 with cleaner record and ray sections. For explanations see text.

By comparing these different records one can conclude:

- The first arriving longitudinal PKPdf waves (dark blue and steeply incident ray travelling through the inner Earth core), which oscillate in the direction of ray propagation, are best recorded on short-period vertical component records of high magnification. The same applies to the surface reflections of P (PP for the shorter way and PP2 for the longer opposite way of travel) and to PcPPKP.
- In contrast to P waves, shear waves, which oscillate perpendicular to the direction of propagation, can travel only through the Earth mantle and crust but not through the liquid outer core. They are best recorded in long-period horizontal component records. And if they contain only horizontally oscillating SH wave energy then they can be seen only in T-component records and not at all in the vertical component records. This applies is our record example to the SS phase (see the red ray and travel-time branch).
- If these arrival times increase with distance of the station to the earthquake than the seismic wave fronts arrive in our case from NNE (as for PKPdf, PP and SS), but if they decrease with distance then they arrive from the SSW (as for PP2, PcPPKP and PPP2).

Having understood these basic features of wave propagation, the formation of different seismic phases due to reflection and conversion, and their appearance in seismic records you may now enjoy the first animation by left-mouse click on the bold-blue file name **wendt_nz_qt** either here or by downloading it from the Directory *Download Programs and Files* (see link on the NMSOP-2 front page). Note that the file is very large and the download may take quite some time. Moreover, if you feel that for your purpose or comprehension the movie speed is either to fast or to slow try to catch the cursor running below the movie with a left-button mouse

click. Hold this button pressed and control the movie speed according to the time you need to read the texts and to comprehend the demonstration, or to speed up too slow sections. More explanations for all 10 movies are given in IS 11.3.

2.2 Wave front propagation, travel-time curves and location of near seismic events

Figure 6 is a simplified plot of the propagation of seismic wave fronts (blue circles for P waves and red circles for S waves) in a homogeneous Earth crust, i.e., a crust with constant velocity of wave propagation in all directions away from the seismic source (star). The source position at focal depth h below the Earth surface is termed the hypocenter H and its projection on the surface the epicenter E. Accordingly, the distance on the Earth surface between the epicenter E and the recording station is termed epicenter distance D and the straight line distance between the hypocenter and the station the hypocenter distance R.
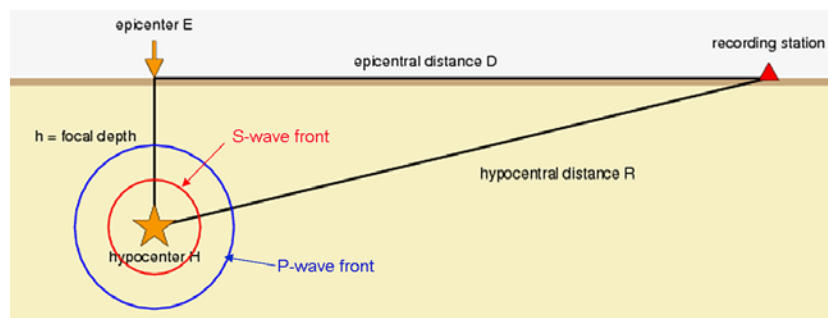

Figure 6 Simplified plot of wave propagation from a seismic source in a homogeneous Earth crust and explanation of terms for characterizing source position and station distance.

The animation shows:
- that in the case of such simplified assumptions about the crustal velocity model the wavefronts of P and S propagate as expanding circles, both in the vertical plane through the source (star) and in the horizontal plane around the epicenter;
- how the seismic records are written on several seismic station sites as soon as the wave fronts arrive,
- how different the amplitudes and amplitude ratios between the first arriving P waves and the later following S waves may look like in the seismic records, and
- how the travel-time curves of P and S as a function of epicenter distance D are formed according to the arrival times of the P and S waves.

This is illustrated in Figure 7 by three screen shots of the movie, taken at different times. The rather smoothly bended travel-time curves shown in the lower row of Figure 7 for P and S waves are average curves for the area assuming a homogeneous crustal velocity model and a source depth of 12.1 km. In contrast, the light colored straight-line curves relate to a source depth of zero kilometers. The onset times for P and S in real records at the different stations may differ up to several tenths of seconds from the theoretical ones due to velocity inhomogeneities in the different directions of wave propagation. When drawing the travel-time curves through the really observed onset times of P and S, these curves would look rather "bumpy", and accordingly the circular wave fronts in the middle and upper row of the screen shots as well. Event location algorithms are based on the least-square minimization of

the difference between observed arrival times of seismic phases and calculated arrival times based on average velocity models. However, without prior detailed investigations we usually do not know much better the real velocity distribution. Then one has to work with the simplified model of circular wavefront propagation. But we should be aware of the possible range of related uncertainties of the location results. They also depend on the number and distance of available recording stations with respect to the seismic source. If, however, we have already a rather detailed knowledge about the 3-D distribution of velocity inhomogeneities by tomographic or other investigations then the number of data to be taken into account in calculating the source location would increase with the third power. Handling such data requires huge data storage and super high-speed data processing facilities But our tutorial and related animation demonstrates that even with simplified assumption reasonably good seismic source locations can already be made by applying a **circle and chord method,** which can be performed even by hand (for details see EX 11.1).
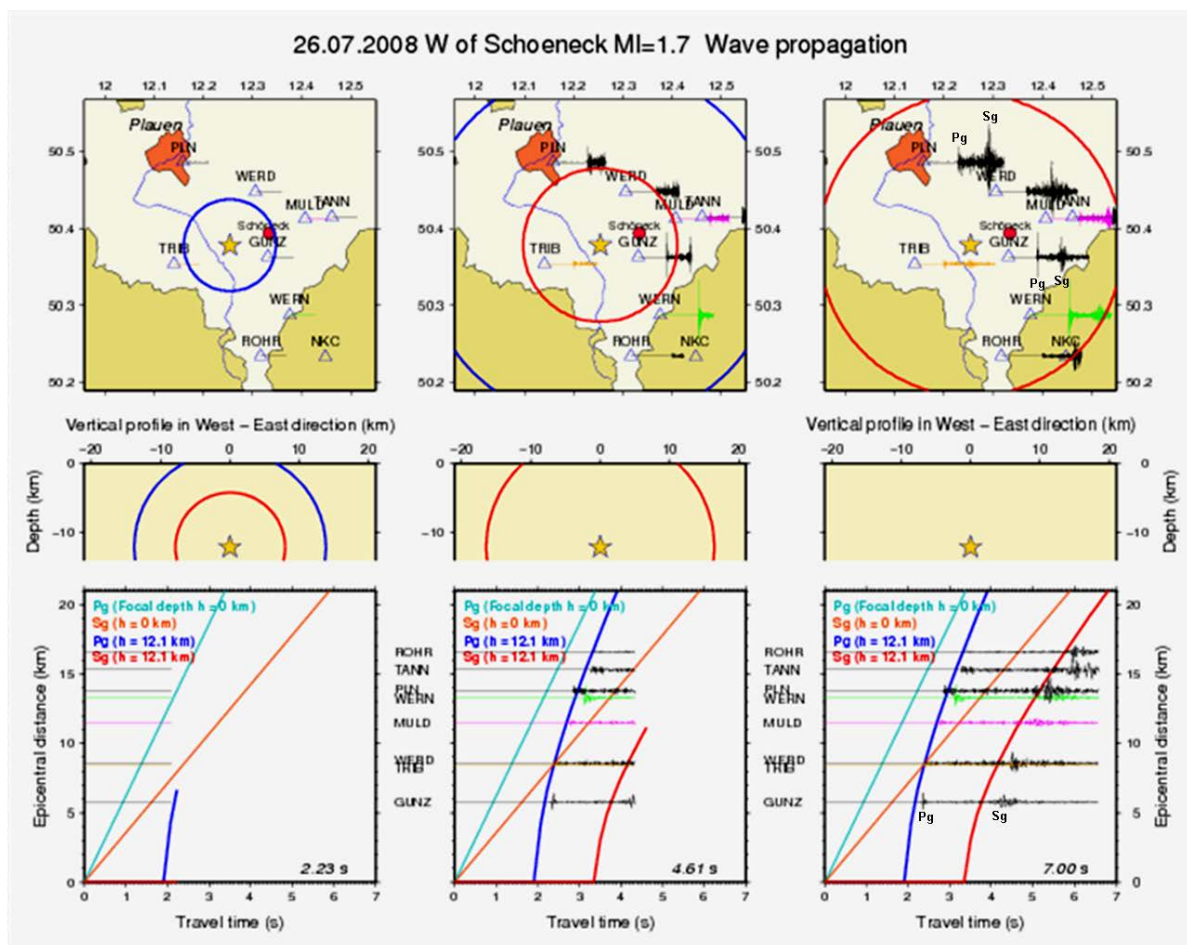
Figure 7   Screen shots of the movie about P- and S-wave propagation from a small earthquake in Germany with magnitude Ml = 1.7, recorded in the local distance range up to 20 km. **Upper row:** Horizontal circular expansion of the of P (blue) and S (red) wavefronts and the related short-period seismic records at stations of a local seismic network. Note the strong variation of the amplitude ratio between P and S waves at different stations. **Middle row:** Vertical circular expansion of the P and S wavefronts. **Lower row.** Light blue and red linear curves: Theoretical travel-time curves for P and S waves from a source at depth h = 0 km; dark blue and red: theoretically expected travel-time curves for P and S waves radiated by a source at 12.1 km depth, superimposed by short-period records at seismic stations as a function of epicenter distance. Download and activate the movie by left-mouse click on the file name **3D-wave-prop_travel-time_qt.**

For carrying out the circle and chord exercise one has to know that longitudinal P waves travel roughly $\sqrt{3}$ times faster than transverse S waves. Further that in continental areas the crustal thickness is on average about 30-35 km thick. For shallow crustal earthquakes Pg is then the first arriving longitudinal wave and Sg the first arriving transverse wave up to distances of about 5 times the crustal thickness (see Figure 1). The difference of arrival times, t(Sg – Pg) measured in seconds, increases more or less linear with hypocenter distance R in kilometers according to the relationship

$$R = t(Sg – Pg)[(v_P \cdot v_S)/(v_P - v_S)].$$

R can thus roughly be estimated when v_P and v_S are known. Assuming for Pg in a homogeneous crust a constant average velocity v_P = 5.9 km/s and thus for Sg of $v_S \approx v_P/\sqrt{3} \approx$ 3.4 km/s then **R $\approx$ 8× t(Sg-Pg)**. This is the commonly assumed "rule-of-thumb". However, for events in the region considered in Figure 7 v_P = 6.2 km/s yields better locations. Accordingly, R = 8.3 × t(Sg-Pg) would then be more appropriate.

For h > 0 R is generally larger than the epicenter distance. R = D holds only for either h = 0 or D >> h ($\rightarrow$ asymptotic approximation).

Measuring t(Sg-Pg) on records of at least 3 stations allows a rough source location by drawing circles with radii R_i around the stations. However, since for h > 0 km D < R the circles do not intersect at the epicenter but overshoot. Only their chords, i.e., the straight lines connecting the two overcrossings between different pairs of circles (Figure 8 right) intersect close to the epicenter.
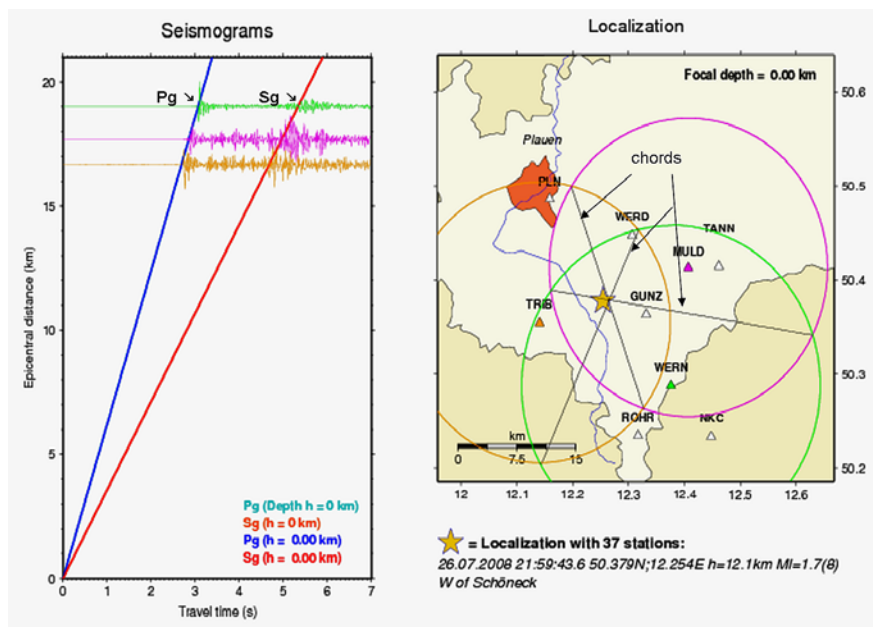
Figure 8 Left: Average linear travel-time curves for P and S from a surface source (h = 0 km) in the Vogtland swarm earthquake region in the South of Eastern Germany and their best match with 3 seismic records at stations of the local Vogtland network at epicenter distances of 16.7, 17.7 and 19.0 km, respectively. **Right:** Circles drawn around the stations with the radii according to the epicenter distances estimated from the left-hand diagram, together with the three chords drawn between the crossing points of overshooting circle. The chords intersect close to the epicenter.

When matching the onset times of the Pg and Sg wave groups recorded at three stations in the near source area with the average linear travel-time curves for P and S waves from a surface source one would estimate epicenter distances of 16.7, 17.7 and 19.0 km, respectively (Figure 8 left). When drawing circles with these radii around the respective stations they strongly overshoot. The circle overshoot, however, is a strong indicator for a finite source depth, which is the deeper the larger the overshoot. By step-wise increase of h, the calculated epicenter distance radii d_i decrease (see Figure 9) until for $d_{i\ min}$ the "true" (better: the most likely) source depth h_{true} can approximately be estimated via the relationship

$$d_{i\ min} = (R_i^2 - h_{true}^2)^{-2}.$$

The circles drawn around the stations i with $d_{i\ min}$ for "h_{true}" are expected to have minimum overshoot (see Figure 9), provided that the wave propagation conditions are sufficiently homogeneous and well represented by the assumed velocity model, and further, that the reading errors of phase onset times on the station records are negligible.

For seeing and downloading the whole movie click with the left mouse button on the file name **wendt_waveprop_circles** either here, or in the list of *Download programs and files*.
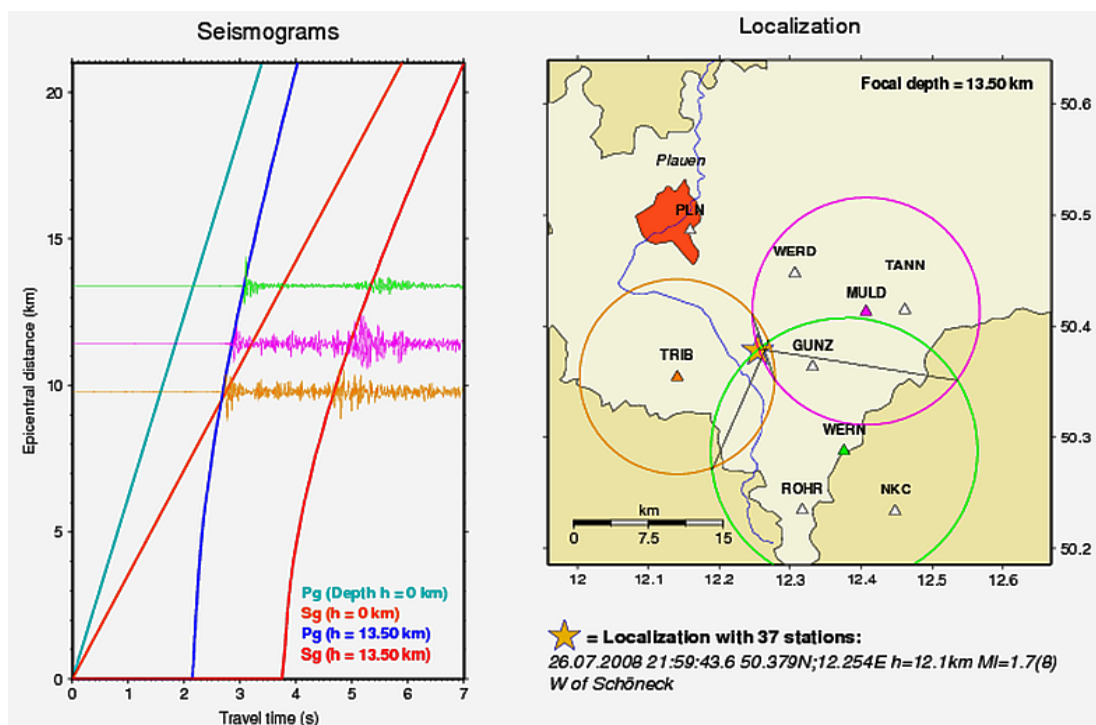

Figure 9 The minimum circle overshoot is achieved for "h_{true}" = 13.5 km, corresponding to circle radii of epicenter distances of 9.8, 11.4 and 13.4 km, respectively.

2.3 Presentation of earthquake sequences in their space-time-magnitude development

Earthquake swarms and aftershock sequences of large earthquakes may consist of hundreds to thousands of events within a limited area, occuring within a relatively short time span with more or less clear spatial relationship to the activated regional seismotectonic features. Moreover, sometimes such sequences are characterized by specific event-number-magnitude-

frequency time plots (Figure 10) and may also show pronounced spatial migration. In order to facilitate a well structured comprehensive analysis of such a multitude of features suitable forms of data presentation are highly desirable, both in the form of 2-D diagrams or projections of 3-D hypocenter clouds as well as their viewing from different perspectives.
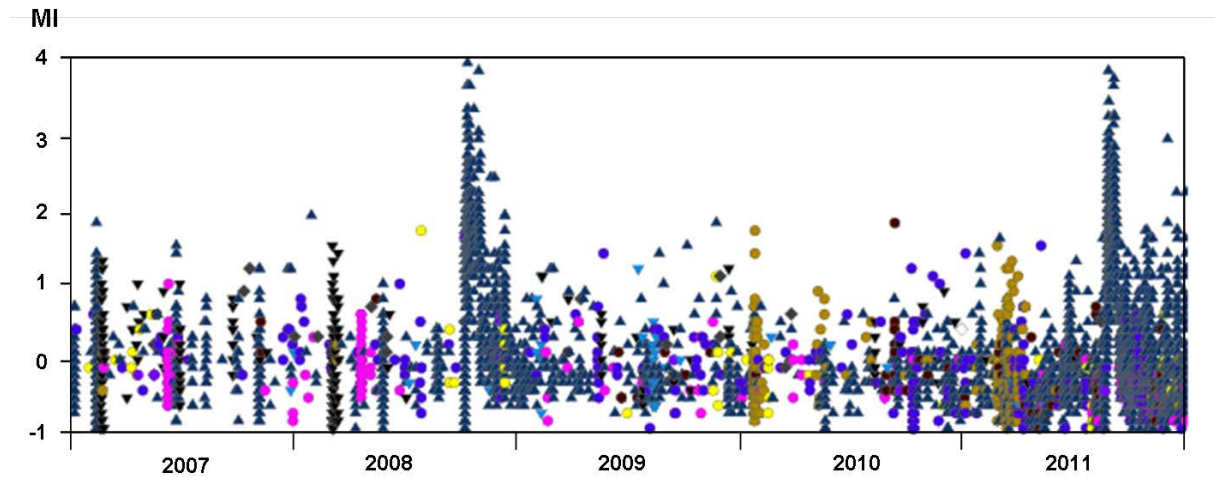

Figure 10 Local magnitude Ml frequency of occurrence of swarm and individual earthquakes in the Vogtland/Germany (dots) and Western Bohemia/Czechia (triangles) region (see Figure 11) between January 1, 2007, and Dezember 31, 2011. Different colors relate to different subregions. Total number of earthquakes 5392.

The animation illustrates this by way of example of an earthquake swarm that occurred between October and December 2008 in Western Bohemia/Czechia. Figure 11 shows the wider area of this source region and the inserted box frame delimitates the area of the specific swarm dealt with in our animation. The total number of detected events in this swarm was 8500 in the magnitude range -1 < Ml < 4. The epicenters fall within an area of only some 6 km in length and 1.5-2.5 km in width. During this swarm a south-to-northward migration of the foci has been observed with gradually decreasing focal depth from initially about 9.5 km to 4.5 km and slight changes in the dominating strike and dip direction of the activated local fault system as inferred from the cumulative clustering of hypocenters (see Figure 12).

To ease the comprehension of these developments in time, the epi- and hypocenters have been assigned different color, ranging from dark blue in early October to bright red in late December 2008 and then been projected to vertical cut planes through the 3-D event cloud along different profiles. The size of the event circles differs with magnitude. The dominating strike direction of the activated fault system can be inferred from the main axis through the epicentre cloud and the related fault dip from the main axis of the best aligned hypocenter projection plot. The latter can best be found by *"walking around"* the source area and looking at vertical profile projections from different view angles (see open arrow in the animation).. The animation illustrates this. Activate and/or download the movie by left-button-mouse click on the bold-blue file name **wendt_source_migra_around** either here or in the listing of *Download programs and files*, which can be opened via *overview* on the front page of NMSOP-2.
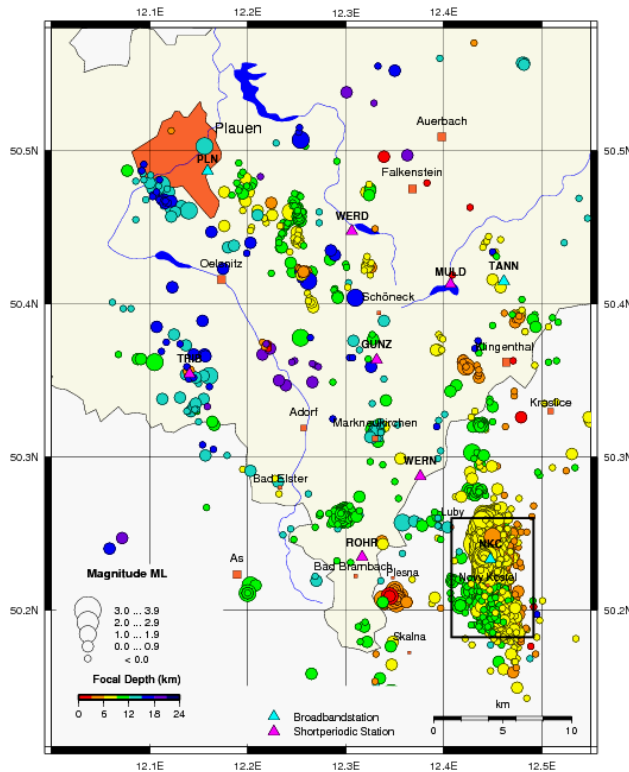
Figure 11 Epicenter map of the earthquake region Vogtland/Germany and Western Bohemia/Czechia. The inserted box in the lower right part delimitates the area of the earthquake swarm in Czechia between October and December 2008 in Figure 10.
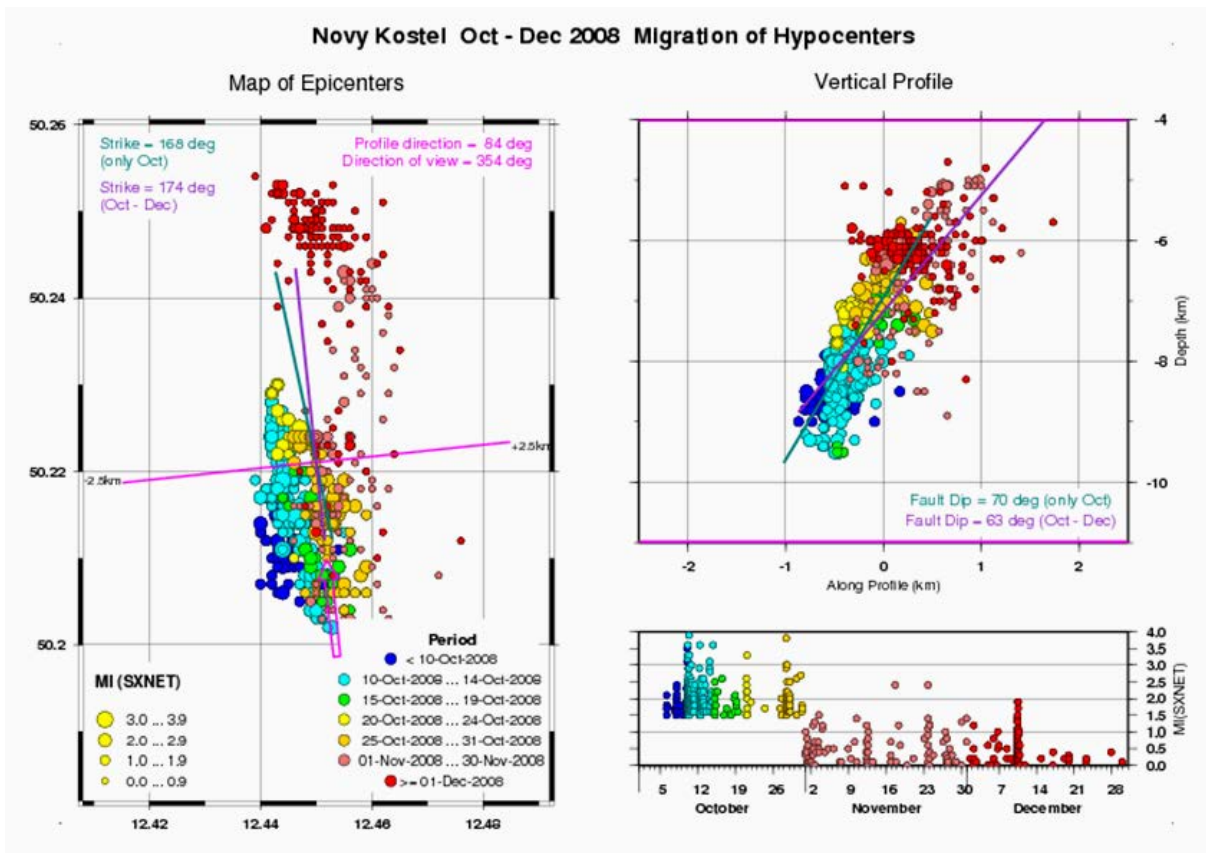

Figure 12 Left: Epicenter plot of the earthquake swarm. **Upper right:** hypocenters projected to the vertical plane of the near E-W profile in the epicentre plot. **Lower right:** Event-number-magnitude development with time for Ml > 1.5 (during October), respectively Ml > 0 during November and December 2008.

In summary, the respective data plots yield a kind of regional cumulative fault plane solution for the earthquake swarm as a whole or of its sub-phases in time. For the main phase in October 2008 the inferred strike direction of the activated fault system is about 168° from North and the fault dip is about 70° towards west. The average strike direction for the total swarm was about 174° with a dip of 63°.

2.4   Radiation patterns of earthquake fault mechanisms

In the event of an earthquake the two adjacent rock formations on both sides of the earthquake fault move relatively to each in opposite direction (see Figure 14, the open arrows). The released elastic strain energy generates both near-source kinematic energy, and the kinematic energy in the source region that propagates as seismic waves to the far field. The seismic waves consist of longitudinal motions in the direction of wave propagation (P waves) and transverse motions perpendicular to the direction of wave propagation (S waves). In the case of S waves the transverse motion may be separated into two components, namely motion in the vertical plane, as in Figure 13, termed SV, and those in the horizontal plane, termed SH.
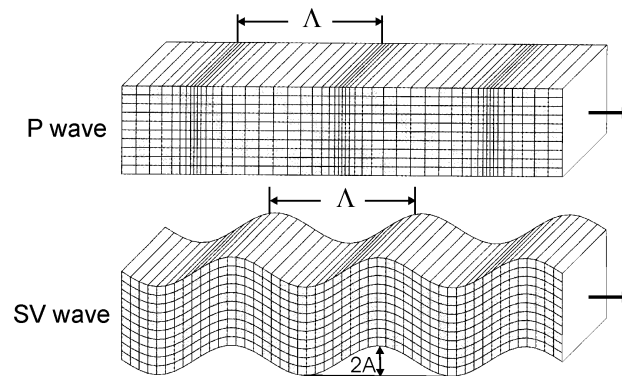
Figure 13 Displacement patterns of a harmonic plane P wave (top) and SV wave (bottom) propagating in a homogeneous isotropic medium. Λ is the wavelength and 2A means double amplitude. The white surface on the right is a segment of the propagating plane wavefront where all particles undergo the same motion at a given instant in time, i.e., they oscillate *in phase*. The arrows indicate the seismic rays, defined as the *normal* to the wavefront, which points in the direction of propagation. (Copied from Fig. 2.6 in Chapter 2, modified according to Shearer, Introduction to Seismology, 1999; with permission from Cambridge Univ. Press).

Earthquake shear ruptures show a typical radiation pattern, which is different for P and S waves. These patterns are characterized by so-called amplitude lobes, i.e., by azimuth-dependent radiation of amplitudes, respectively energy. In the case of a pure shear rupture in a homogeneous isotropic medium P-waves have the smallest (idealized zero) amplitudes in the direction of fault rupture and the largest amplitudes (see black arrows in Figure 11, left side) at an angle 45° off the fault plane whereas shear (S) waves have the largest amplitudes in the direction of the shear rupture and perpendicular to it. Joint analysis of P and S wave amplitudes, and especially of the amplitude ratios of P/SV and P/SH, is – although a quite complicated procedure - a powerful method to identify the type of earthquake rupture, to reliably constrain its orientation in space and to quantify its defining parameters with an even

smaller number of observations points and less complete azimuthal coverage than required when only P-wave first motion polarities are used.
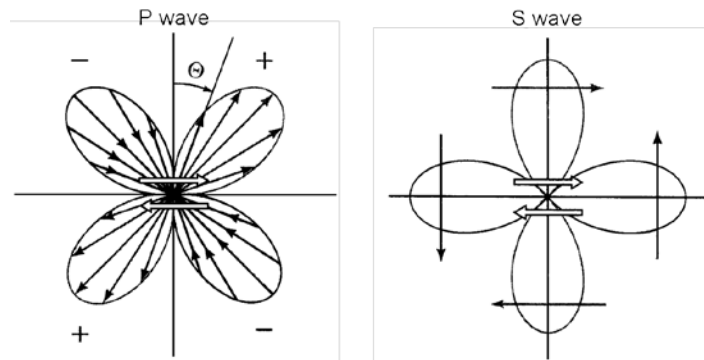

Figure 14 Diagrams of the radiation pattern of the radial displacement component of P-waves (left) and of the transverse displacement component of S waves (right) from a double couple shear rupture (Modified combination of Figures 4.5 and 4.6 of Aki and Richards, 2002; with permission of P. Richards).

One recognizes from Figure 14 (left-hand panel) that the longitudinal source displacement is outward directed in the upper right and lower left quadrant. Accordingly, the related P waves arrive at seismic stations as a compression signal which produces in vertical component records an upward first motion (+). In contrast, in the two other quadrants, 90° away from the + quadrants, the longitudinal displacement is directed towards the source (dilatation). Accordingly, the P-wave first motion in vertical component records is downward (-). Therefore, the most simple and most frequently used method of determining the seismic source mechanism is to investigate the azimuthal distribution of first motion polarities observed at seismic stations surrounding the seismic source in all directions (see EX 3.2). However, small earthquakes are commonly recorded in narrowband filtered seismic records of high magnification. Due to the rather pronounced transient response of such records the first motion amplitudes may be significantly smaller than the largest amplitudes in the P waveforms and be distorted or even buried in the seismic noise (see Chapter 4, Figs. 4.9 and 4.10 and Chapter 16, Fig. 16.25). Therefore, one requires many more and azimuthally well distributed P-wave polarity readings than P/S wave amplitude ratios in order to produce a well constrained fault plane solution. Also, maximum amplitudes in the P- and S-waveforms can still reliably be read if the P-wave first motion is already buried in the noise.

According to Figure 14 a fault which ruptures perpendicular to the horizontally plotted fault rupture would produce the same radiation pattern. Therefore, analyzing only P-wave polarity distributions will not allow to say, which of the two possible faults has really ruptured. Therefore, in this kind of an idealized point source rupture model according to a double-couple shear force system (see black arrows in the right S-wave panel of Figure 14) the amplitude radiation lobes have been symmetrically mirrored. Yet, this ambiguity which of the two potential fault planes is really the acting one is a principle one, independent on whether one analyzes the P- or S-wave radiation pattern or that of the P/S-wave amplitude ratios. In practice it can only be resolved by assessing either the directivity effects (see Figure 19 and related comments), or the distribution of aftershocks, or by invoking geological information (tectonic setting, mapped faults; see solutions of EX 3.2).

The key parameters which control the orientation and slip of a fault in space and thus the observed radiation pattern of P- and S-wave amplitudes are (see Figure 15):

• strike angle ϕ (measured clockwise from north);

• dip angle δ (measured downwards from the horizontal;

• rake angle λ, which describes the slip direction (values between 0° and 180° for upward motion or between 0° and -180° for downward motion of the hanging/overlaying wall.
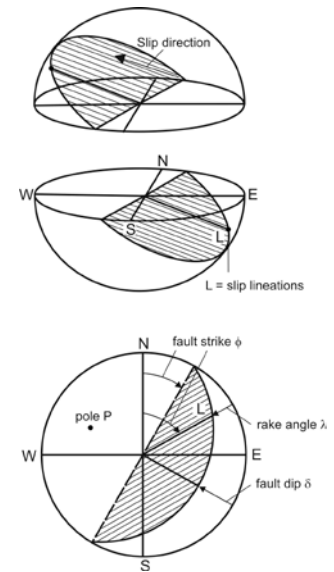

Figure 15   Idealized rupture plane with slip lineations surrounded by an imagined so-called "focal sphere" centered in the origin. **Top:** upper hemisphere, **middle:** lower hemisphere; **bottom:** projection of the lower focal hemisphere fault plane onto the horizontal plane between the two hemispheres. The block of the Earth medium above the fault plane is termed the "hanging wall", that below the "foot wall".

According to the relationship between these three fault-plane parameters one classifies earthquake ruptures into 3 basic types and related mixed types. In seismological publications they are usually presented as the projections of the fault plane cut traces through the focal sphere onto the horizontal plane between the upper and lower focal hemisphere and by coloring or shading differently the quadrants with compressional and dilatational first P-wave motions. Such presentations of fault plane solutions are also nick-named as "beach-ball solutions" (see Figure 16).
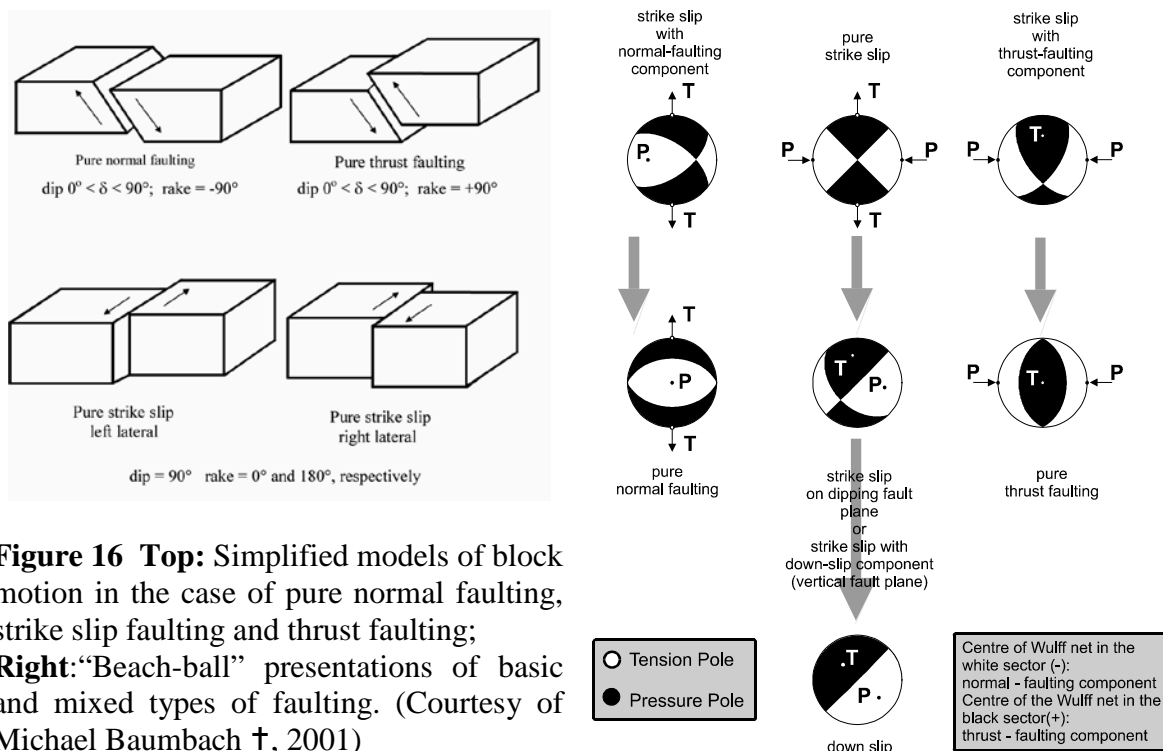
Figure 16 Top: Simplified models of block motion in the case of pure normal faulting, strike slip faulting and thrust faulting;
Right:"Beach-ball" presentations of basic and mixed types of faulting. (Courtesy of Michael Baumbach †, 2001)

As compared to Figure 14, the amplitude radiation patterns for P and S waves observed on the Earth surface from earthquake ruptures with different fault-plane and slip orientation in space are rather asymmetric. This could be shown for a well constrained fault plane solution of a Vogtland earthquake in Germany with known strike, dip and rake. The radiation lobes (also for the animation examples) have been calculated by using the formulas (4.89) to (4.91) published by Aki and Richards (2002). No assumptions with respect to *source directivity*, rupture velocity or type of slip (e.g., unilateral, bi-lateral, circular) have made (see final discussion below). The agreement with the actually recorded amplitude ratios measured at stations of a local network is remarkably good. E.g., for the station TRIB the calculations predict for PV a very small amplitude but a slightly larger SV amplitude. In contrast, as observed, PV should be larger than SV for station GUNZ (Figure 17). This concerns the expected amplitude ratios, not the absolute amplitudes. The latter additionally depend on epicenter distance, local site amplification effects and other factors.
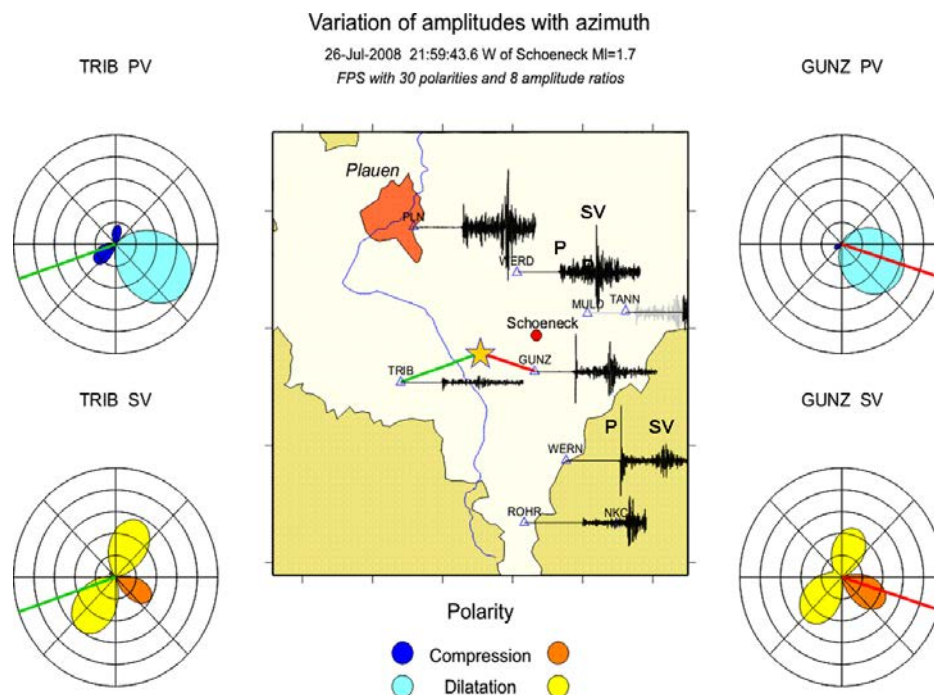
Figure 17 Comparison of theoretically calculated radiation patterns for an earthquake with well constrained fault plane solution and slip direction with the really observed amplitude ratios between vertical component P and S amplitudes at stations of a local seismic network in Germany. The source depth of the earthquake has been 12.1 km and the epicenter (respectively hypocenter) distances of stations GUNZ and TRIB were 5.8 km (13.4 km) and 8.5 km (14.7 km).

The azimuth-dependent PV, SV, SH amplitude lobe patterns depend on the **strike, dip and rake** and thus on the type of source mechanism of the acting fault plane. But with respect to the seismic stations which record these amplitudes the lobe size and patterns also depend on the incidence angle of the seismic rays. This is shown with the first animation, while in the following animations, which demonstrate the effect of variations in dip and rake, the incidence angle at the recording stations has been kept fixed. The movie with several of such

animations can be viewed and/or downloaded by left mouse-button click on the file name **wendt_source_rad_pat** either here or in the listing *Download programs and files*. After downloading Linux users should activate the movie by typing after the command **xanim** the file name **wendt_source_rad_pat**. Figure 18 presents two snap shots from this movie.
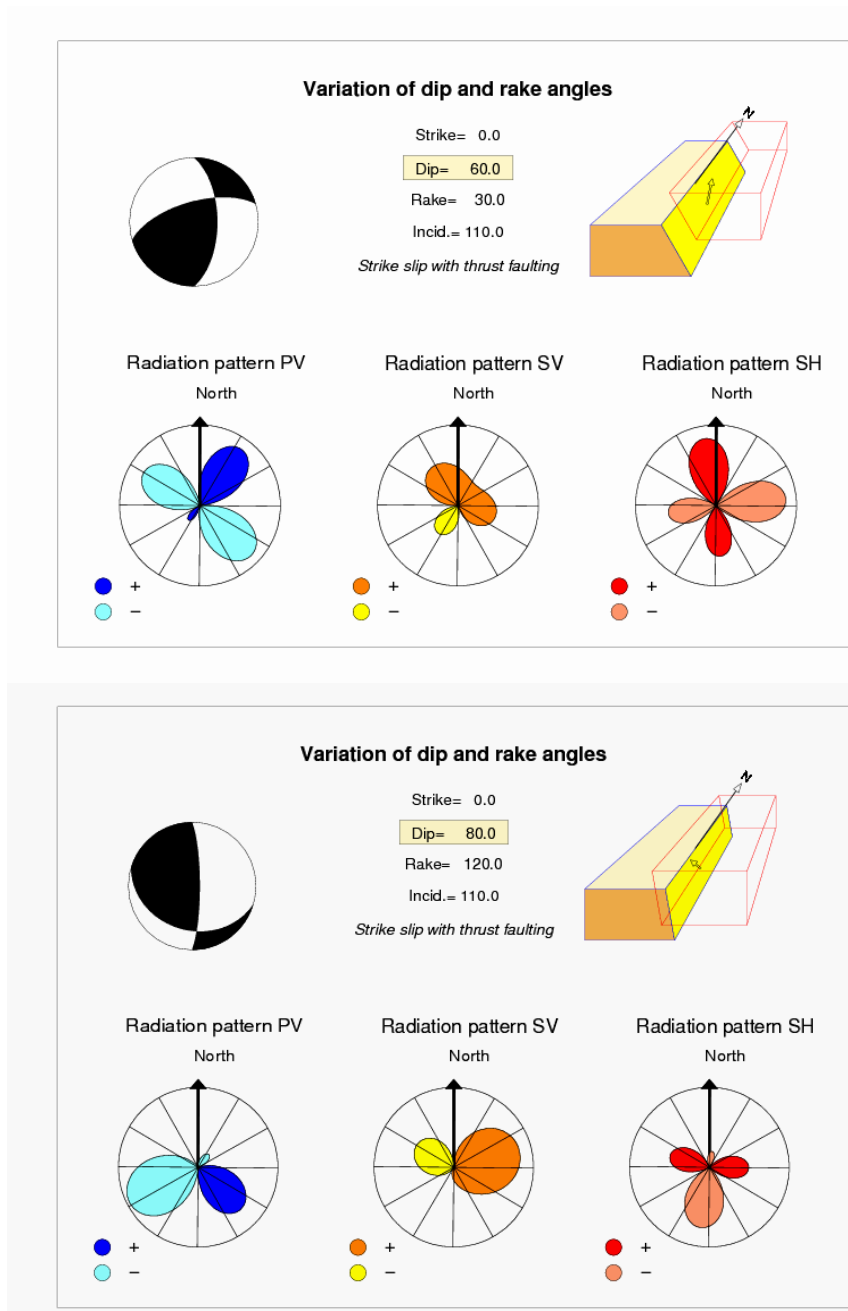

Figure 18 Cut-out scenes of the movie **wendt_source_rad_pat** for dip and rake variations.

In all these calculations, source directivity has been neglected. According to the NMSOP-2 Glossary, the term directivity is defined as: "*An effect of a propagating fault rupture whereby the amplitudes and frequency of the generated ground motions depend on the direction of wave propagation with respect to fault orientation, slip direction(s) and rupture velocity v_r. The directivity and thus the radiation pattern is different for P and S waves.*" It becomes more pronounced when v_r approaches the respective wave velocity. Accordingly, it is larger

for S than for P waves. This is illustrated by Figure 19. v_R commonly ranges between about 0.2 and 0.9 times of the shear-wave velocity v_s (Venkataraman and Kanamori, 2004b). Yet, in rare cases, it may even exceed v_s if the hypothesis and still debated occasional observational evidence of supershear slip pulses with rupture velocities up to 5 km/s really holds (e.g., Bouchon and Vallée, 2003).
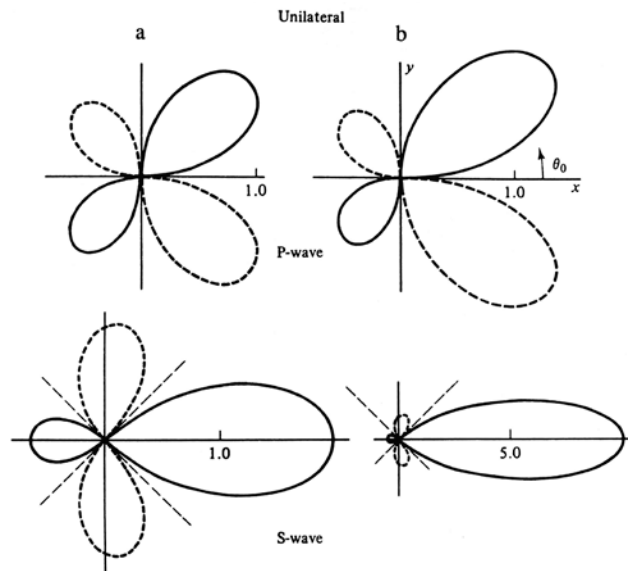
Figure 19 Variability of P- and SH-wave amplitude for a fault rupture propagating unilaterally from left to right with $v_r/v_S = 0.5$ (left column) and $v_r/v_S = 0.9$ (right column), respectively.
(From Kasahara, 1981; © Cambridge University Press).

In the directions of enlarged amplitudes the recorded broadband pulse width of P and S (or source time function) is compressed, in the directions of reduced amplitudes, however, stretched, i.e., the apparent rupture duration is azimuth dependent. Yet the area underneath the pulses, which is proportional to the seismic moment of the fault rupture, remains constant, i.e., it is independent on the azimuth of observation.

Pronounced directivity effects are observed for extended (finite linear in contrast to point source) ruptures of strong earthquakes, primarily in the case of unilateral rupture propagation. The azimuthal effects, however, are much less in the case of bilateral ruptures and disappear in the case of circular ruptures. Only in rare cases the effects of vertical directivity have been observed. (See related discussions and Figures in Lay and Wallace, 1995). The frequency dependence is due to the Doppler-effect. It can be quantified by investigating the azimuth-dependence of the frequency spectra of the recorded P and S waves. Thus, in the case of distinct directivity effects one can unambiguously identify, which of the two potential rupture planes has really moved.

For small local events, however, recorded at rather high frequencies, directivity effects can usually be neglected. E.g., in the case of the earthquake in Figure 17 with Ml = 1.7 the source radius has been estimated to be about 0.1 km only, when assuming a circular rupture according to the Brune (1970) or Madariaga (1976) models (see EX 3.4). Moreover, according to Cho et al. (2010), observations suggest that directivity effects are generally present only at frequencies less than about 1 Hz, whereas the records presented in Figure 17 consist only of frequencies above 6 Hz. At high frequencies, the directivity effect is generally reduced and the radiation pattern observed in the far-field (i.e., at distances of several wavelengths, as in our case) changes from the usual double-couple pattern as in Figure 14 to a more isotropic one. Such differences in the radiation patterns between high and low frequency

ground motion have already earlier been explained as either a source effect (with real sources loosing coherence at short wavelengths associated with source roughness/irregularities that are not considered in planar fault models) or as a multi-pathing effect (with high frequency waves being preferentially scattered by crustal heterogeneities (e.g., Newmann and Okal, 1998) or a combination of both (Bormann and Di Giacomo, 2011).

In summary, if spatially extended earthquakes do not, as in Figure 19, propagate unilaterally but bilateral or in an even more complex manner (as, e.g., the Chile earthquake 2010 in section 2.6), radiation patterns may look different from those presented here. They may even vary with time during great ruptures that last for several minutes.

2.5 Rupture tracking of the great 2004 Mw9.3 Sumatra-Andaman earthquake

This is a pure movie without accompanying text. It illustrates the variability of energy release in space and time by great earthquake ruptures which can not be described by a point source or otherwise simplified rupture models. The movie has kindly been made available by Matthias Ohrnberger. It relates to the publication in Nature by Krüger and Ohrnberger (2005) about rupture tracking of the great 26 December 2004 Sumatra-Andaman tsunamigenic earthquake by using the German Regional Seismic Network as a large-scale teleseismic array (see Figure 20). The movie illustrates that such a great earthquake with variable rupture trend, rupture velocity and energy release in different rupture segments can really not be described reasonably well by a common single source fault-plane solution. Tsai et al. (2005) have later approximated this earthquake by a more realistic multi source rupture with 5 major sub-sources.
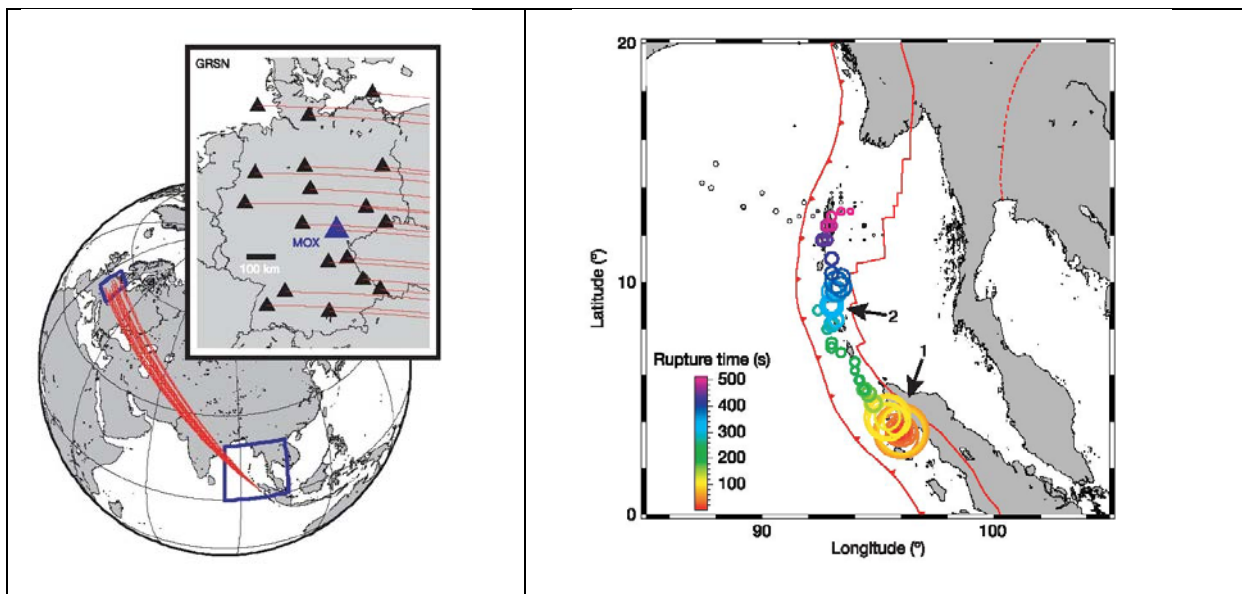

Figure 20 **Left:** Ray paths from the source area of the Sumatra-Andaman earthquake to Germany and, in the insert, the outlay of stations of the German Regional Seismic Network (GRSN) that has been used as a large-scale teleseismic array for tracking the rupture. **Right:** Rupture propagation as a function of time with the radius of the circles being proportional to the seismic energy released. Combined Figures 1 and 3 of Krüger and Ohrnberger (2005), Nature, 435, p.937 and 938; doi: 10.1038/nature0396 (© Copyright Clearing Centre of Nature).

For activating and/or downloading of the movie click with the left mouse button on the file name **ohrnberger_sumatra2004_rupture** proceed as described above.

2.6 Rupture tracking of the great 2010 Mw8.8 Chile earthquake

A similarly strong damaging earthquake occurred in Chile on 27 February 2010. Its rupture process has been tracked by Yanlu Ma of the GFZ German Research Centre for Geosciences by applying a similar procedure described by Krüger and Ohrnberger (2005). He used travel-time delays observed at North American seismic stations, mainly of the USArray, yet including some other permanent stations, e.g., of the California network, as well.

In contrast to the Sumatra earthquake, which can be described as a unilateral rupture, the centers of large seismic energy release during this Chile earthquake jump forth and back, making it to a multilateral rupture. This animation illustrates well how irrelevant in such a case parameters such as epicenter location, average displacement, average stress drop, average rupture velocity or similar are with respect to assessing the hazard posed by such an extended earthquake rupture.
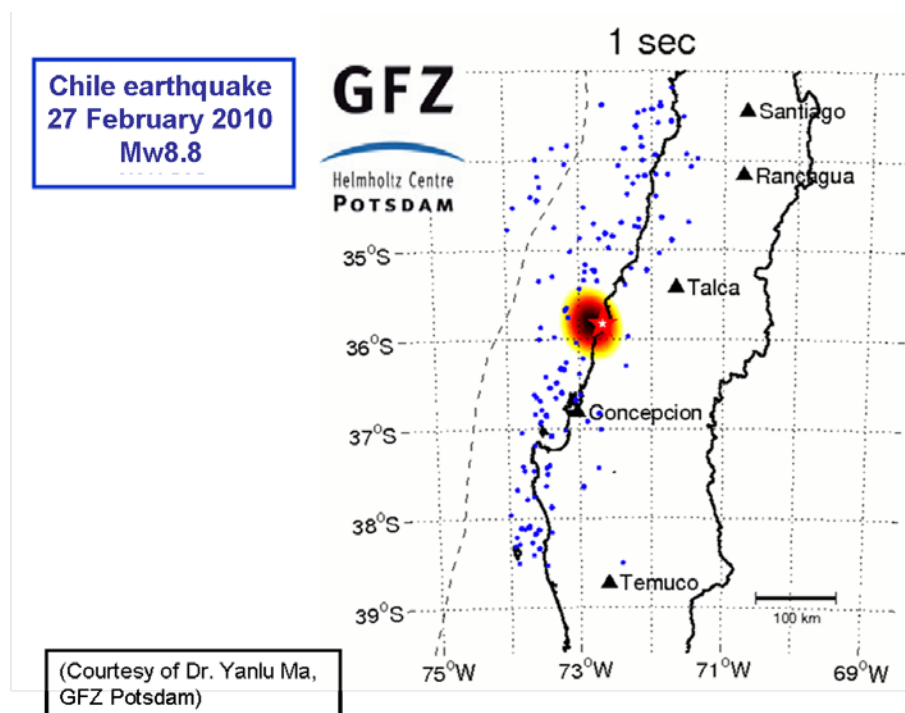
Figure 20 Map of area of the great Chile earthquake of 2010. Blue dots: epicentres of aftershock within the first few days. Red star: epicentre of the main shock. The colored areas cover the 95% confidence region of seismic energy release of major sub-events of this complex rupture.

Activate/download this movie with the left-button mouse click on the file name **gfz_ma_chile2010_rupture** here or in the directory *Download programs and files* (see overview on the NMSOP-2 front page).

References

Aki, K., and Richards, P. G. (2002). *Quantitative seismology*. 2nd edition, University Science Books, Sausalito, CA.,xvii + 700 pp.

Bormann, P., and D. Di Giacomo (2011). The moment magnitude M_w and the energy magnitude M_e: common roots and differences. *J. Seismology*, **15**, 411-427; doi: 10.1007/s10950-010-9219-2.

Bouchon, M., and Vallée, M. (2003). Observation of long supershear rupture during the magnitude 8.1 Kunlunshan earthquake. *Science*, **301**, 824-826.

Brune, J. N. (1970). Tectonic stress and the spectra of shear vaves from earthquakes. *J. Geophy. Res.*, **75**, 4997-5009.

Cho, H., Hu, J., Klinger, Y., and Dunham, E. M. (2010). Frequency dependence of radiation patterns and directivity effects in ground motion from earthquakes on rough faults. Am. Geophys. Union, Fall Meeting 2010, abstract #S51A-1914.

Kasahara, K. (1981). *Earthquake mechanics*. Cambridge University Press, Cambridge, UK.

Kennett, B. L. N., Engdahl, E. R., and Buland, R. (1995). Constraints on seismic velocities in the Earth from traveltimes. *Geophys. J. Int*., **122**, 108-124.

Lay, T., and Wallace, T. C. (1995). Modern global seismology. ISBN 0-12-732870-X, *Academic Press*, 521 pp.

Madariaga, R. (1976). Dynamics of an expanding circular fault. *Bull. Seism. Soc. Am.*, **66**, 639-666.

Montagner, J.-P., and Kennett, B. L. N. (1996). How to reconcile body-wave and normal-mode reference Earth models? *Geophys. J. Int*., **125**, 229-248.

Newman, A. V., and Okal, E. A. (1998). Teleseismic estimates of radiated seismic energy: The E/M_o discriminant for tsunami earthquakes. *J. Geophys. Res*., **103**, 26,885-26,897.

Krüger F., and Ohrnberger, M. (2005). Tracking the rupture of the Mw = 9.3 Sumatra earthquake over 1,150 km at teleseismic distances. *Nature*, 435, 937-939: doi: 10.1038/nature03696.

Tsai, V. C., Nettles, M., Ekström, G., and Dziewonski, A. (2005). Multiple CMT source analysis of the 2004 Sumatra earthquake. *Geophysical Research Letters*, **32**; L17304, doi: 10.1029/2005GL023813.

Venkataraman, A, and H. Kanamori (2004a). Observational constraints on the fracture energy of subduction zone earthquakes, *J. Geophys. Res.* **109**, B04301, doi: 0431.01029JB002549.